

The Dynamics of Wave-Induced Downslope Winds

J. B. KLEMP AND D. K. LILLY

National Center for Atmospheric Research,¹ Boulder, Colo. 80303

(Manuscript received 10 June 1974, in revised form 28 August 1974)

ABSTRACT

A theory for the dynamics of strong surface winds on the lee side of a large mountain range is derived and compared with observations. The strong winds observed near Boulder, Colo., are found to be surface manifestations of standing gravity waves whose wavelength is long compared to typical resonant lee wavelengths. The theory indicates that such waves can become very intense if an inversion is present near mountain-top level in the upstream environment and if the stability and wind profiles are such that the waves approximately reverse phase between the surface and the tropopause. The theory is extended to the development of a numerical model for estimation of maximum surface winds from upstream sounding data. Comparisons of the model predictions with observations are sufficiently encouraging to suggest the future utilization of such a model for operational forecasting. The differences between the predictions of this theory and those of hydraulic jump models are explored.

1. Introduction

Strong downslope winds, often gusting to well above nominal hurricane force (34 m s^{-1}) are observed in many mountainous regions of the world. The generation of such winds has in the past been primarily attributed to one of two rather different types of disturbances possible in stably stratified flow. Scorer and Klieforth (1959), Aanenson (1965) and others have attributed them to rather short (generally $< 20 \text{ km}$ wavelength) quasi-periodic lee waves. These waves form downstream of a mountain range under conditions which allow trapping of wave energy, in particular when the wind speed increases rapidly with height. Other investigators (Kuettner, 1959; Houghton and Isaacson, 1968; Arakawa, 1969) have described the wind storm phenomenon on the basis of hydraulic jump theory, assuming the atmosphere can be modelled as two or more neutrally stratified layers with sharp inversions at each layer interface.

Observations of downslope windstorms in the vicinity of Boulder, Colo., indicate that the storms are associated with waves of horizontal wavelength of order 50–100 km, essentially forced by the contours of the mountain, and propagating freely in the vertical. Trapped resonant waves do not appear to play an important role in the phenomenon. In this article we describe a mechanism for the generation of downslope winds which is different from both the trapped lee wave and hydraulic jump theories. Our analysis is, how-

ever, developed from familiar concepts of wave dynamics in a continuously stratified medium. It is described most simply within the context of a linear, two-dimensional, steady-state hydrostatic model of forced wave motion in a multi-layered atmosphere, and is most closely related to the analysis of Eliassen and Palm (1960).

To explain some of the motivation behind this analysis, we begin in Section 2 by summarizing the relevant observational data relating to downslope windstorms. In Section 3 we obtain analytic solutions for simple linear multi-layer models, which are then used to identify the upstream atmospheric conditions responsible for the generation of intense surface winds. These optimal conditions are interpreted in terms of partial reflection of vertically-propagating wave energy. In Section 4 observed windstorm data are compared with the results of a linear numerical wave model run with the corresponding real atmospheric sounding data. Finally, in Section 5, we compare our results with those of hydraulic jump models. Although the jump concept cannot be completely dismissed from consideration, we conclude that our model appears to be more realistic in its assumptions and predictions.

2. Downslope windstorm observations

Brinkmann (1973) has observed that mountain winds have historically been classified in terms of thermal effects rather than wind intensity. As a result, authors would describe the characteristics of foehn winds or chinooks (warm winds) and boras (cold winds) with little or no mention of the associated surface wind

¹ The National Center for Atmospheric Research is sponsored by the National Science Foundation.

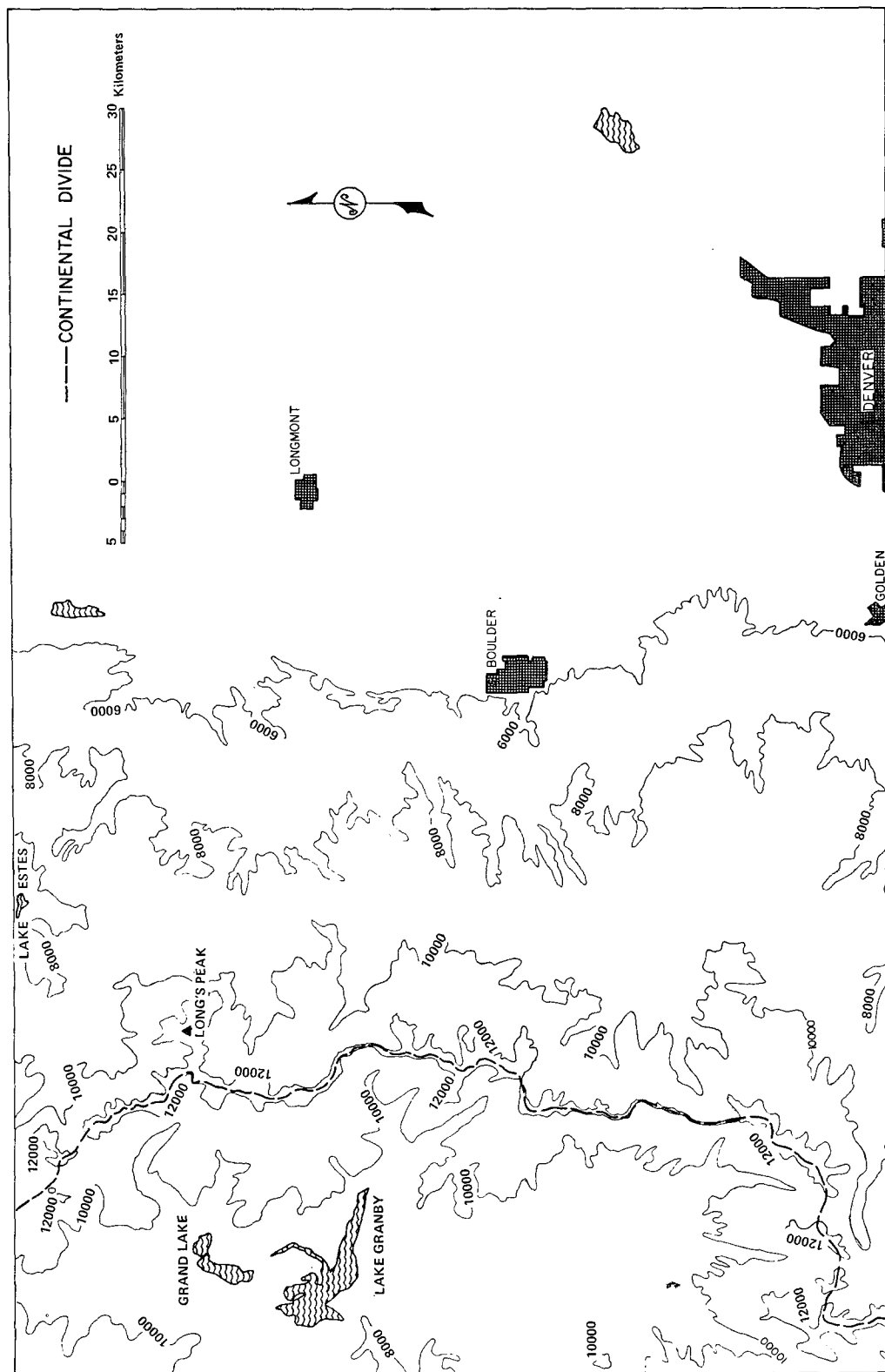


FIG. 1. Mountain topography in the vicinity of Boulder, Colo. Altitudes are in feet (10,000 ft = 3280 m).

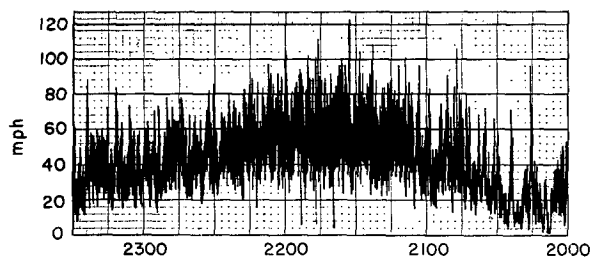


FIG. 2. Anemometer trace from Southern Hills Junior High School on 11 January 1972 from 2000–2330 MST. The school is in a populated area of Boulder, about 1 mi east of the base of the foothills. Time runs from right to left. The wind speed is given in miles per hour ($1 \text{ mph} = 0.45 \text{ m s}^{-1}$).

speeds. Detailed observations of the surface wind and the overlying atmosphere have only more recently begun to appear in the literature.

The principal observational data which have stimulated this theoretical investigation come from the eastern slope of the Rocky Mountains near Boulder and Denver. This is a region of unusually severe and frequent downslope windstorms which have been previously discussed by Julian and Julian (1969), Lilly and Zipser (1972), and most recently and extensively by Brinkmann (1973). Because of the high population density (and high density of meteorologists), there is a relatively complete documentation of windstorms in this area.

Downslope windstorms with similar characteristics are also found in various other parts of the world. Brinkmann notes that this phenomenon has been reported in Altdorf, Switzerland, in Mendoza, Argentina (Georgii, 1954), in Trieste, Yugoslavia (Yoshino, 1971), and in several locations in Hokkaido, the northern island of Japan (Arakawa, 1969). In addition, it has been reported that the Pennine hills of northeast England produce strong lee slope amplification of westerly gales (Aanensen, 1965).

Along the eastern slope of the Rocky Mountains, the region of the most frequently reported intense downslope windstorms is in the immediate vicinity of Boulder. Fig. 1 shows that Boulder is located at the immediate eastern foot of a ridge of mountains having an average maximum height of 2 km above the flat plain to the east. This ridge extends quite uniformly along a north-south line about 50 km in length. It then continues less uniformly, but as a barrier essentially unbroken for about 100 km to the north and 400 km to the south. The Boulder area is almost unique in the Colorado Rockies in its proximity (30 km) to such a high and well defined ridge to the west with level plains to the east. Air impinging on this barrier from the west and northwest has not previously passed over any range of similar altitude for several hundred kilometers, but winds coming from the southwest or north-northwest must cross other large mountain ranges immediately upwind and then pass more obliquely over the

north-south ridge. Most downslope windstorms in the Boulder area are associated with strong westerly or northwesterly flow at mountain-top levels. Such conditions occur during the winter months when the static stability in the lower troposphere is also somewhat greater than normal. We believe that all of the above factors—the well-defined north-south ridge with flat terrain immediately downwind, the frequent exposure to strong westerly winds, and the increased static stability—combine to produce the observed high frequency of intense downslope winds.

Because of the high population density in the Boulder area, severe windstorms cause considerable property damage. Although the wind intensity depends to some extent on small-scale terrain effects and exposure, relatively exposed sites typically experience gusts above nominal hurricane force several times each winter, while storms with gusts above 50 m s^{-1} occur every year or two. During such windstorms there can be substantial damage to roofs and windows of buildings, mobile homes, partially-completed construction, and generally to any thing that is not very sturdy or not tied down. For example, in a particularly severe windstorm on 11 January 1972, damage in the Boulder area was estimated at about \$2 million. Fig. 2 shows an anemograph trace recorded during this storm from the roof of a low building by a three-cup anemometer of standard rugged design and rather slow response. Brinkmann has shown that the extreme gustiness observed in this trace is typical of such storms in Boulder and also of those in other parts of the world.

During these windstorms the region of strong wind intensity appears to be highly localized along the base

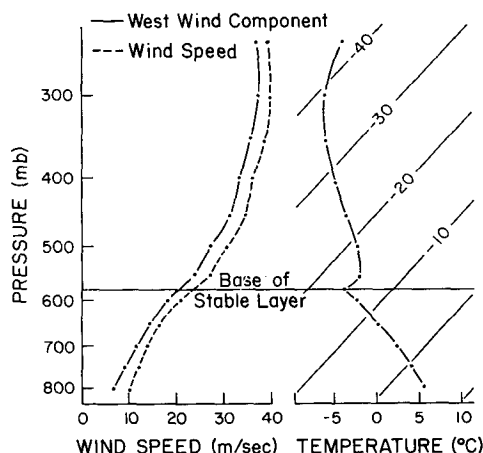


FIG. 3. Composite upwind sounding for the 20 windstorm cases analyzed by Brinkmann (1973). The individual soundings were taken from the National Weather Service rawinsonde station in the most appropriate upwind direction at the time nearest the beginning of the windstorm. To avoid smoothing out the inversion usually found near mountain-top level the soundings were adjusted vertically before averaging so that the inversion bases all lay at the level of their modal average, about 580 mb. Mountain-top level here is about 650 mb.

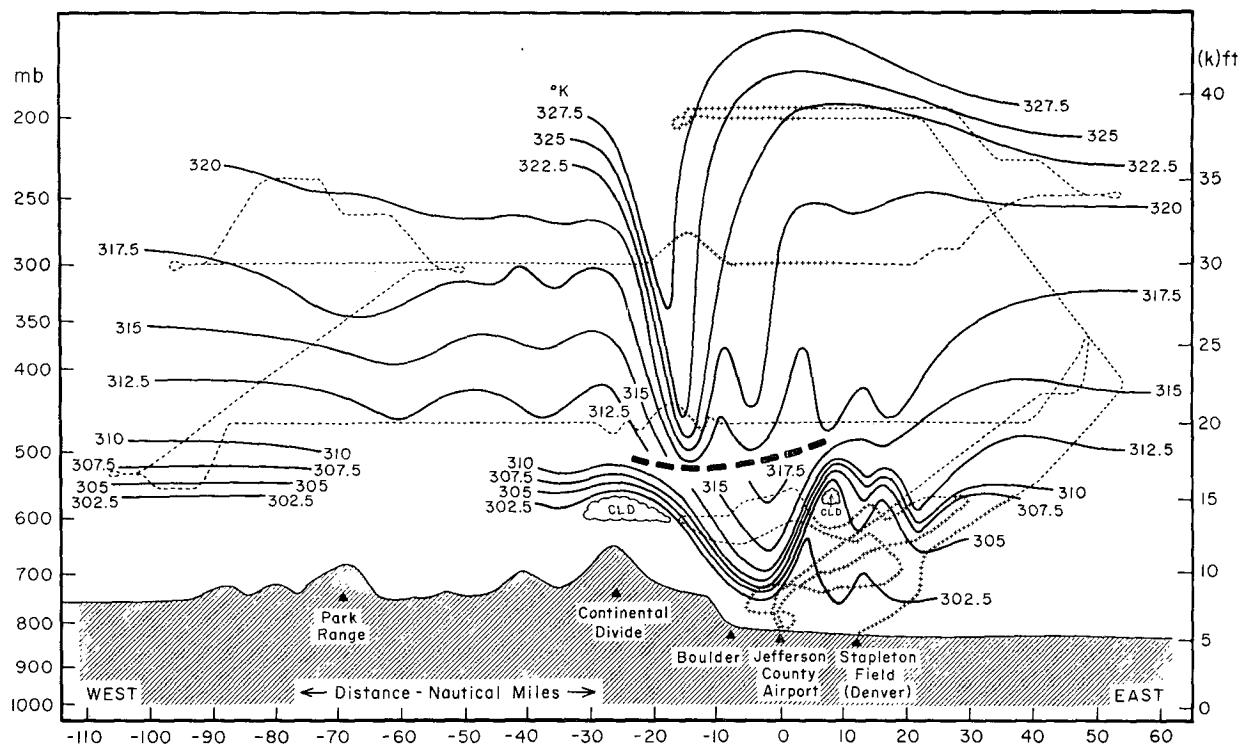


FIG. 4. Cross section of the potential temperature field (K) along an east-west line through Boulder, as obtained from analysis of the Queen Air and Sabreliner data on 11 January 1972. For steady adiabatic flow, these isentropes are good indicators of the streamlines of the air motion. Data above the heavy dashed line are from the Sabreliner, taken between 1700 and 2000 MST, while those below this line are primarily from the Queen Air taken from 1330 to 1500. Flight tracks are indicated by the dashed lines, except for crosses in turbulent portions. For further details, see Lilly and Zipser (1972).

of the lee slope. Plotting the wind speed recorded at various anemometer stations in an east-west line during periods of strong windstorms in Boulder, Brinkmann observed a sharp maximum in wind speed at Boulder with winds decreasing rapidly and monotonically to the east. Arakawa (1969) also emphasizes this point, noting that at several locations in Hokkaido, Japan, heavy windstorm damage is localized to regions within about 4 km of the base of the mountains.

The upper air structure of downslope windstorms has been much less well documented than their surface manifestations. It appears to be generally true that these storms coincide with strong, though not extreme, flow velocities across the mountain ranges throughout the troposphere. Brinkmann exhibited mean soundings (Fig. 3) associated with Boulder windstorms, taken from the nearest (in space and time) upwind rawin station. Although these soundings are seldom close enough for great confidence, this composite of some 20 windstorm cases clearly indicates the presence of an inversion or stable layer in the lower troposphere in which the wind speed is quite strong. For these cases the mean height of the inversion base is 580 mb, which is about 70 mb above mountaintop level. Aanensen (1965) in England and Arakawa (1969) in Japan also emphasize the existence of this low-level inversion

during windstorm periods. However, winds in the upper troposphere are not unusually strong. Brinkmann points out that the maximum surface gusts recorded in Boulder are frequently stronger than the mean wind speed at any level in the troposphere upstream of the mountains.

In recent years, research aircraft from the National Center for Atmospheric Research (NCAR) have observed and recorded the structure of the atmosphere above the eastern slope of the Rockies during windstorm and near-windstorm conditions on several occasions. The most spectacular of these observations occurred on 11 January 1972 [first described by Lilly and Zipser (1972)] for which cross sections of potential temperature and westerly wind speed are shown in Figs. 4 and 5. These figures illustrate the strikingly large-amplitude and long-wavelength oscillation associated with such storms and are typical of the other less extreme cases. The heavy dashed line in Fig. 4 separates the data collected by the two NCAR aircraft. An interval of about 4 h separated these two flights, which accounts for some shifting in the position of the large-amplitude wave. The high-altitude flight from which Fig. 5 was constructed occurred during a period when the surface wind maximum was located upstream of Boulder. A more detailed analysis of these aircraft

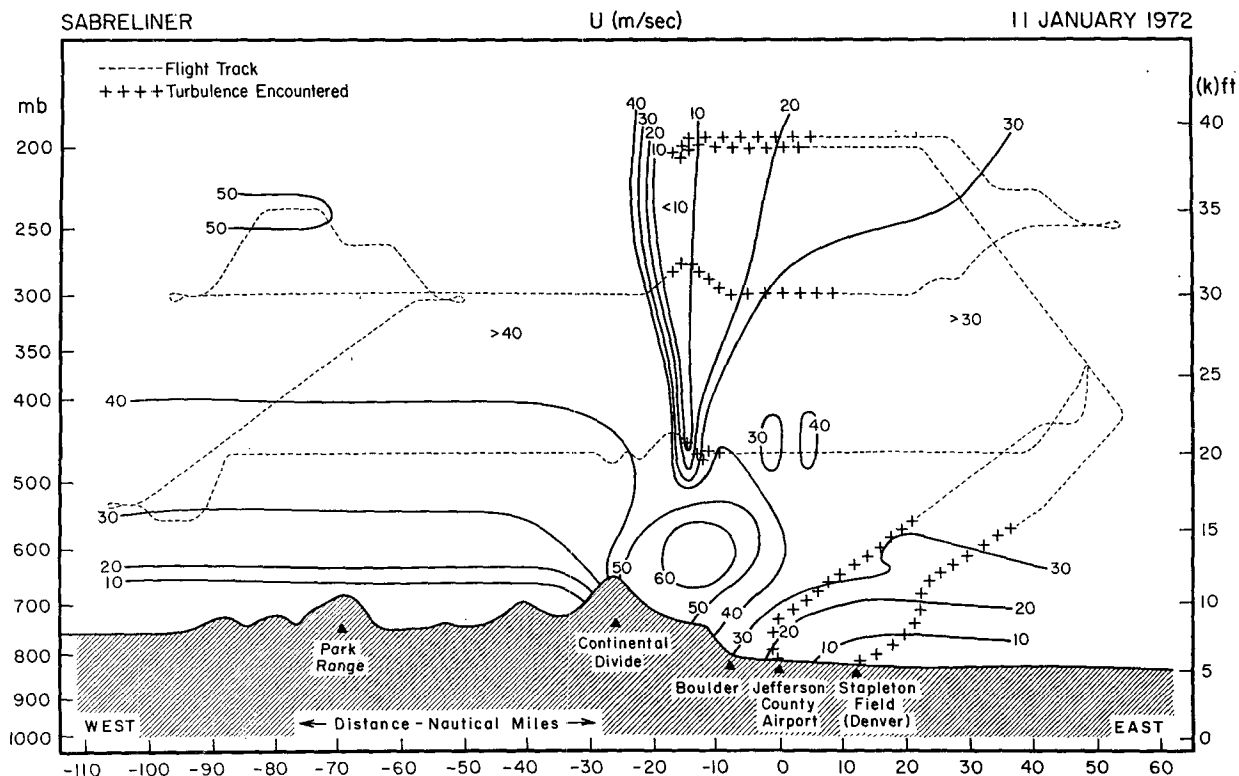


FIG. 5. Contours of horizontal velocity (m s^{-1}) along the same cross section as in Fig. 4, as derived from the Sabreliner data only. The analysis below 500 mb was partially obtained from vertical integration of the continuity equation, assuming two-dimensional steady-state flow.

measurements, to be presented elsewhere, indicates that a large downward flux of horizontal momentum was associated with this wave. Thus, although some evidence of resonance wave motion is apparent in Fig. 4, the dominant, large-amplitude wave is apparently an untrapped mode forced directly by the mountain contour. Because of the large characteristic width of the mountain ridge, it appears that this wave motion may be nearly hydrostatic. Other observations in Boulder and elsewhere which show a single wind maximum located at the base of the mountain, are also consistent with the surface wind profile that would be generated by an untrapped, forced mode.

During the 11 January 1972 windstorm, the atmosphere immediately downstream of the streamline trough at most levels of the troposphere contained turbulence which ranged from moderate to nearly extreme in intensity. These data suggest that strong damping forces are acting, which prevent the wave from attaining even greater amplitude.

3. Analysis of linear multi-layer models

The observations described above suggest that the atmosphere upstream of a windstorm rather consistently displays a region of increased stability and strong flow slightly above mountain-top level, and wind speeds in the upper troposphere which are not excep-

tionally large. With these characteristics in mind, we consider the results of linear multi-layer models designed to determine the structure of the incident flow which produces maximum amplification of the down-slope surface winds. For simplicity, we restrict our analysis to incompressible Boussinesq flow, but the results are essentially valid for a compressible atmosphere if we replace density by potential density or the inverse of potential temperature. In addition, the flow is assumed to be two-dimensional, which appears to be a good approximation to the situation along the eastern slope of the Colorado Rocky Mountains and in various other regions where this phenomenon occurs.

For all cases in which the linear model generates a large-amplitude response, nonlinear effects can be expected to be significant. In addition, physical instability and subsequent breakdown of the wave motion undoubtedly reduces the amplitude from what is predicted in the absence of these effects. The purpose of this investigation is, however, to identify the atmospheric conditions capable of producing large-amplitude wave motion and the associated downslope windstorms. In this regard we feel that linear theory is of great value in locating and understanding the situations which generate strong response, although the actual amplitude predicted is likely to be overestimated.

a. Basic three-layer model

To begin, we shall analyze the linear, steady-state, two-dimensional wave motion generated in an incompressible, three-layer atmosphere. Resonant modes are not considered, and although some nonhydrostatic effects will be discussed, solutions will be primarily derived for the hydrostatic case, since this approximation appears to be valid in many windstorm situations. To investigate the atmospheric conditions capable of producing a strong response, we shall obtain solutions for flow over a single Fourier component of a mountain contour; if the solution for a particular mountain shape is desired, it can be readily constructed using Fourier transforms. We assume that the mean stability N is constant within each layer, and thus with three layers it is possible to represent the essential features of an atmosphere (illustrated in Fig. 6) in which there is a low-level stable layer, a less stable troposphere, and a stable stratosphere above the tropopause located at $z = z_2$. A four-layer model, in which a thin region of relatively low stability is included beneath the inversion layer, is considered in Section 3g. Solutions will be derived which allow linear wind shear in the lowest two layers, as shown in Fig. 6, although the case of small shear will be emphasized in interpreting the results. One could also allow for variations in the mean wind speed by specifying a constant but different mean wind in each of the three layers. However, following this procedure produces some artificial effects in the resulting solution, caused by the discontinuities in the mean wind across the interfaces between layers. Such discontinuities are subject to shearing instabilities and cannot, therefore, persist. For these reasons only continuous wind profiles will be considered in this analysis.

Utilizing the Boussinesq approximation, the linear, hydrostatic, steady-state equation for the vertical velocity w becomes

$$\frac{\partial^2 w}{\partial z^2} + l^2 w = 0,$$

where for an atmosphere with linear vertical shear, the Scorer parameter l is defined by

$$l^2 = -\frac{g}{U^2} \frac{\partial \ln \bar{\rho}}{\partial z} \frac{N^2}{U^2},$$

with N equal to the Brunt-Väisälä frequency. To obtain the solution for a single Fourier component, let

$$[u(x, z), w(x, z)] = [\hat{u}(z), \hat{w}(z)] e^{ikx}.$$

Consequently, the equation for $\hat{w}(z)$ in each layer is simply

$$\frac{d^2 \hat{w}_i}{dz^2} + \frac{N_i^2}{U_i^2 [1 + \alpha_i(z - z_{i-1})]^2} \hat{w}_i = 0, \quad (1)$$

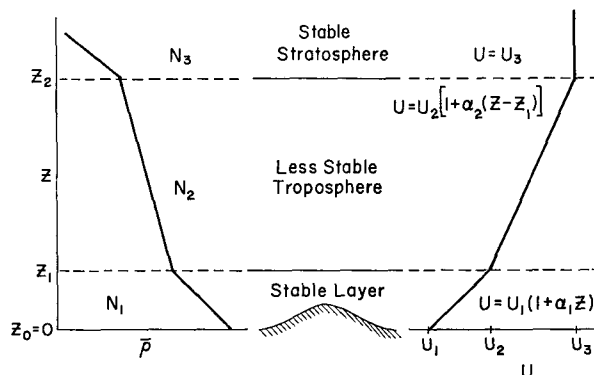


FIG. 6. Density and velocity profiles in a three-layer incompressible atmosphere with constant stability and linear shear in each layer. The three layers represent an idealized atmosphere having a low-level stable region (layer 1), a less stable troposphere (layer 2), and a stable stratosphere (layer 3). In an incompressible atmosphere the stability is defined as $N^2 = -g(\partial \ln \rho / \partial z)$, while in the compressible analogue it is given by $N^2 = g(\partial \ln \theta / \partial z)$.

where $i = 1, 2, 3$ denotes the respective layer, U_i is the mean wind velocity at the bottom of each layer, and $U_i \alpha_i$ the shear of the layer. Solutions to this equation are of the form

$$\hat{w}_i(\delta_i) = e^{\alpha_i \delta_i / 2} (a_i \cos \mu_i \delta_i + b_i \sin \mu_i \delta_i), \quad i = 1, 2, 3, \quad (2)$$

where

$$\left. \begin{aligned} \delta_i &= -\frac{1}{\alpha_i} \ln [1 + \alpha_i(z - z_{i-1})] \\ \mu_i^2 &= \frac{N_i^2}{U_i^2} - \frac{\alpha_i^2}{4} = l_i^2 \left(1 - \frac{1}{4R_i} \right) \end{aligned} \right\}.$$

Here, $R_i = N_i^2 / (\alpha_i^2 U_i^2)$ represents the mean Richardson number in each layer and $l_i = N_i / U_i$. Note that if the wind shear vanishes in any given layer, the independent variable δ_i reduces to $\delta_i = z - z_{i-1}$.

To complete the solution to Eqs. (1), we must determine the complex constants, a_i and b_i , by applying the appropriate boundary conditions and matching conditions at interfaces between layers. At the lower boundary, the Fourier representation of the surface contour is $\zeta_0(x) = H e^{ikx}$, where H is the mountain amplitude, and thus

$$\hat{w}_1(0) = ik U_1 H. \quad (3)$$

The boundary condition at the top of the model, though conventional, is worth some discussion. Observations (Lilly and Kennedy, 1973) indicate that waves having small horizontal wavenumber k tend to propagate up through the troposphere and then break down somewhere in the lower stratosphere with little apparent reflection of wave energy. With this in mind,

we impose a restriction in our uppermost layer which allows wave energy to propagate upward without reflection. Assuming $\alpha_3=0$, this radiation-type boundary condition requires that the solution in the top layer satisfy the relationship (Eliassen and Palm, 1960)

$$\frac{d\hat{w}_3}{dz} = i \operatorname{sgn}(k) l_3 \hat{w}_3. \quad (4)$$

This condition leads to solutions in the lowest two layers which allow upward transport of wave energy and downward transport of momentum. At the interfaces between layers, the displacement height and the pressure along this surface must match, and these re-

quirements yield the matching conditions

$$\left. \begin{aligned} \hat{w}_i(z_i) &= \hat{w}_{i+1}(z_i) \\ \frac{\partial \hat{w}_i(z_i)}{\partial z} &= \frac{\partial \hat{w}_{i+1}(z_i)}{\partial z} - \left(\alpha_{i+1} - \frac{U_i}{U_{i+1}} \alpha_i \right) \hat{w}_{i+1}(z_i) \end{aligned} \right\}, \quad (5)$$

which are applied for $i=1, 2$. The complete solution is then obtained from Eqs. (2) subject to the constraints (3), (4) and (5).

In order to determine the maximum velocity generated at the surface, we seek the solution for wave motion in the lowest layer of the model. This is derived in the manner described above and yields the following expressions for a_1 and b_1 :

$$\left. \begin{aligned} a_1 &= ikU_1H \\ b_1 &= ikU_1H \frac{U_1\mu_1 \sin\phi_1 + (\frac{1}{2}N_1R_1^{-\frac{1}{2}} - \frac{1}{2}N_2R_2^{-\frac{1}{2}} + U_2\mu_2\beta) \cos\phi_1}{U_1\mu_1 \cos\phi_1 - (\frac{1}{2}N_1R_1^{-\frac{1}{2}} - \frac{1}{2}N_2R_2^{-\frac{1}{2}} + U_2\mu_2\beta) \sin\phi_1} \end{aligned} \right\}, \quad (6)$$

where

$$\beta = \frac{U_2\mu_2 \sin\phi_2 + (\frac{1}{2}N_2R_2^{-\frac{1}{2}} + iN_3) \cos\phi_2}{U_2\mu_2 \cos\phi_2 - (\frac{1}{2}N_2R_2^{-\frac{1}{2}} + iN_3) \sin\phi_2},$$

$$\phi_i = \mu_i \Delta_i,$$

$$\Delta_i = \frac{1}{\alpha_i} \ln[1 + \alpha_i(z_i - z_{i-1})] = \frac{U_i \ln(U_{i+1}/U_i)}{U_{i+1} - U_i} (z_i - z_{i-1}).$$

Here ϕ_i , $i=1, 2$, represents the phase shift of the wave motion across layer i . Using the continuity equation and (2), we find that the maximum perturbation wind speed at the surface has the form

$$|\hat{u}(0)| = \frac{1}{kU_1} |U_1\mu_1 b_1 + \frac{1}{2}N_1R_1^{-\frac{1}{2}} a_1|. \quad (7)$$

Thus, after specifying the atmospheric structure within the framework of the three-layer system, we may determine the maximum surface winds by evaluating (6) and (7).

b. Weak-shear assumption

Because of the complexity of the expressions for b_1 and β , it is instructive to consider solutions for the case of small shear. With this simplification the essential physics of the problem are retained and it is possible to examine the conditions capable of generating a strong response in some detail. Thus, for the present we shall assume that R_1 and R_2 are much greater than unity, so that terms involving R_1 and R_2 are neglected in the expressions for μ , β and $\hat{u}(0)$. Note that although

the shear is assumed small within a given layer, the velocity change across the layer need not be small if the layer is relatively thick. For this reason we shall retain the effect of increasing wind speed across a layer in the expression for Δ_i . By following this procedure we include the effect of shear on the optimal thicknesses of the layers but neglect its effect on the resulting maximum surface wind speed. Later in this section we justify and extend these assumptions by considering the exact solutions for cases of stronger shear.

After making the large Richardson number assumption, the expression for the maximum amplitude of the surface wind [Eq. (7)] becomes

$$|\hat{u}(0)| = N_1 H A, \quad A = \left(\frac{X+Y}{X-Y} \right)^{\frac{1}{2}}, \quad (8)$$

where

$$\left. \begin{aligned} X &= (N_2^2 + N_1^2)(N_3^2 + N_2^2) \\ &\quad + (N_2^2 - N_1^2)(N_3^2 - N_2^2) \cos 2\phi_2 \\ Y &= (N_2^2 - N_1^2)(N_3^2 + N_2^2) \cos 2\phi_1 + (N_3^2 - N_2^2) \\ &\quad \times [(N_2^2 + N_1^2) \cos 2\phi_1 \cos 2\phi_2 \\ &\quad - 2N_1 N_2 \sin 2\phi_1 \sin 2\phi_2] \end{aligned} \right\}. \quad (9)$$

For a one-layer atmosphere having constant properties N_1 and U_1 , the maximum perturbation of the horizontal surface velocity is $N_1 H$. Thus, A may be thought of as an amplification factor multiplying the velocity which would be attained in a single layer system having $N=N_1$.

Maximizing this amplification factor A as a function of ϕ_1 and ϕ_2 shows that the strongest response (consistent with lowest stability in the middle layer) is

generated when the atmosphere satisfies the conditions

$$\left. \begin{aligned} \phi_1 &= (n - \frac{1}{2})\pi \quad \text{or} \quad z_1 = (n - \frac{1}{2})\frac{\lambda_1}{2}, \quad n = 1, 2, 3, \dots \\ \phi_2 &= (m - \frac{1}{2})\pi \quad \text{or} \quad z_2 - z_1 = (m - \frac{1}{2})\frac{\lambda_2}{2}, \quad m = 1, 2, 3, \dots \end{aligned} \right\}, \quad (10)$$

where $\lambda_i = (2\pi/\phi_i)(z_i - z_{i-1})$, $i = 1, 2$, represents the average vertical wavelengths of the wave motion in the lowest and middle layers. From observations, and numerical simulations using real data (see Table 1 in Section 4), these predictions are best verified by the cases for which $n = m = 1$. In other words, maximum amplification of the surface velocity in a three-layer system occurs when the lower two layers each have a thickness equaling one-fourth of the vertical wavelength in the respective layer. Since the vertical wavelength is shorter in the more stable layer, this optimal structure is consistent with the presence of a relatively thin, low-level inversion with a thicker, less stable troposphere above.

We believe the observed dominance of the gravest mode ($n = m = 1$) solutions to be principally an effect of nonlinearity and wave breakdown. Some aspects of nonlinearity are discussed in Section 5, while others must be reserved for subsequent papers. It is clear, however, that nonlinear effects must be strong if the perturbation velocity amplitude equals the mean flow at some level, and in fact that is the limiting criterion for overturning instability in the wave. The higher mode solutions inevitably must be associated with weaker mean flows, with the optimal value of U_2 only one-third as strong for $m = 2$ as for $m = 1$. Thus even though Eq. (8) predicts velocity amplitudes dependent only on stabilities and mountain height, the nonlinear effects and breakdown limits are much more restrictive for the higher modes than for $m = n = 1$.

Subject to the conditions described by Eq. (10), the maximum value of the amplification factor becomes

$$A_{\max} = \frac{N_1 N_3}{N_2^2}. \quad (11)$$

Notice that high stability in the low-level inversion (layer 1) and in the stratosphere (layer 3) together with decreased stability in the upper troposphere (layer 2) all serve to enhance the magnitude of A_{\max} . For small rates of shear, the mean velocities in each layer do not explicitly affect A_{\max} . The mean wind speed does play an important role, however, in producing the optimal phase shift across each layer. For example, if $\Delta U_i = U_{i+1} - U_i$ is not too large, the expressions for λ_i , ϕ_i , and Δ_i can be combined to yield

$$\lambda_i = \frac{2\pi}{l_i} \frac{\Delta U_i}{U_i \ln[1 + (\Delta U_i/U_i)]} \approx \frac{2\pi}{N_i} \frac{U_i + U_{i+1}}{2},$$

indicating that the vertical wavelength is roughly proportional to the average mean in a given layer.

A typical strong response solution can be obtained for wind speeds and stabilities in the respective layers given by

$$\left. \begin{aligned} N_1 &= 1.6 \times 10^{-2} \text{ s}^{-1}, & U_1 &= 15 \text{ m s}^{-1} \\ N_2 &= 0.9 \times 10^{-2} \text{ s}^{-1}, & U_2 &= 25 \text{ m s}^{-1} \\ N_3 &= 2.0 \times 10^{-2} \text{ s}^{-1}, & U_3 &= 45 \text{ m s}^{-1} \end{aligned} \right\}. \quad (12)$$

In a compressible atmosphere, these stabilities would correspond to temperature lapse rates of 3 K km⁻¹ in the stable layer and 7.8 K km⁻¹ in the upper troposphere and an isothermal stratosphere. The computed layer depths of optimal response are 1920 m for the stable layer and 5940 m for the upper troposphere, giving a tropopause height of 7860 m above the lowest layer of air which actually passes over the mountain (since some upstream blocking may occur). The computed amplification factor $A = 4.0$, and the predicted maximum perturbation surface velocity for a 500 m sinusoidal mountain (1000 m ridge to trough) is 32 m s⁻¹. The Richardson numbers in both layers are of order 10. Characteristics of this optimal structure are consistent with Brinkmann's observations and with the numerical results presented in Section 4.

It is also of interest to locate the position at which the maximum surface velocity occurs. Deriving the expression for $\hat{u}(0)$ from (2) subject to (6), it can be readily shown that for the optimal three-layer system, the surface velocity has its maximum halfway down the lee side of the sinusoidal surface contour. Of course, downslope windstorms tend to produce the most damage and concern when the region of intense winds occurs near the base of the mountain where the population density may be high. However, during such periods of large-amplitude wave motion, nonlinear effects become significant and act to displace the surface velocity maximum further downstream (to be presented by the authors in a subsequent paper). The effect of non-sinusoidal mountain shape will be illustrated in the next section.

c. Two-layer solution

For comparison, let us briefly consider how the results described above are altered by the absence of the low-level stable region. In this case our model reduces to a two-layer system in which we have only a stable stratosphere (region 3) and a less stable troposphere (region 2). The two-layer expression for $|\hat{u}(0)|$ is again represented by (8) and (9) if we set $N_1 = N_2$ and $\Delta_1 = 0$. This yields

$$\left. \begin{aligned} |\hat{u}(0)| &= N_2 H A \\ A &= \left[\frac{(N_3^2 + N_2^2) + (N_3^2 - N_2^2) \cos 2\phi_2}{(N_3^2 + N_2^2) - (N_3^2 - N_2^2) \cos 2\phi_2} \right]^{\frac{1}{2}} \end{aligned} \right\}. \quad (13)$$

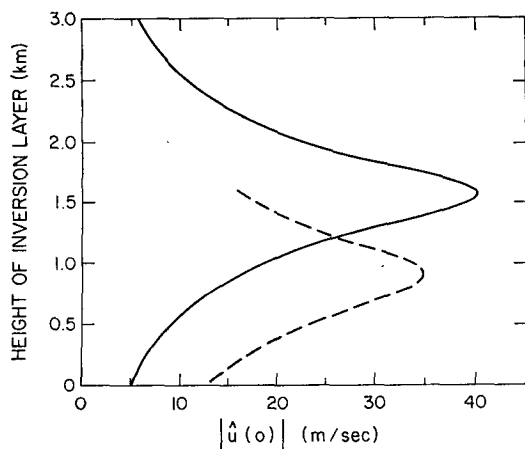


FIG. 7. Variation of maximum perturbation surface velocity with changes in the thickness or height of the low-level stable layer. Solid line represents the three-layer atmosphere with constant stability inversion layer; the dashed line the three-layer atmosphere with a sharp inversion above a neutrally stable layer, described at the end of Section 3.

Here, the maximum value of A is N_3/N_2 , and occurs when $\phi_2 = n\pi$, $n = 1, 2, 3, \dots$. For the most physically meaningful case of $n=1$, this corresponds to the troposphere having a thickness of one-half of its vertical wavelength. This result is consistent with those obtained by Blumen (1965), who found that the momentum flux in a two-layer atmosphere with random topography is greatest when the lower layer is one-half wavelength in thickness. Under these conditions, the optimal $|u'(0)|$ is $N_3 H$, which corresponds to the response generated by a one-layer model having the stability of the stratosphere. By comparison with Eq. (11) we see that the maximum surface velocity for the optimal three-layer model is greater than that for the optimal two-layer system by a factor of N_1^2/N_2^2 . Clearly, in these simple systems, the presence of a low-level stable layer enhances the potential for producing strong surface winds.

d. Sensitivity to parameter variations

To illustrate the sensitivity of the amplitude and position of the maximum surface velocities generated by the three-layer model, we have calculated the resulting maximum surface velocity for a set of atmospheric conditions similar to, though slightly less realistic than, those of the previous example. For this computation we have set $U = 20 \text{ m s}^{-1}$ throughout the inversion layer, and

$$N_1 = N_3 = 0.02 \text{ s}^{-1}, \quad N_2 = 0.01 \text{ s}^{-1}, \quad (14)$$

and again we assume that $R_2 \gg 1$. The stabilities listed above essentially represent an isothermal stable layer and stratosphere, and a middle troposphere having a lapse rate of $\sim 7 \text{ K km}^{-1}$. The surface wind speed, from Eq. (8), is evaluated for a sinusoidal mountain profile

having a ridge-to-trough amplitude of 1 km. The position of the tropopause, z_2 , is fixed at the height it would have in the optimal case in which the lower two layers have quarter wavelength thicknesses, and z_1 is allowed to vary. The resulting maximum perturbation surface velocity is plotted in Fig. 7 (solid line) as a function of the thickness of the low-level stable layer. Notice that $|u'(0)|$ has its maximum amplitude of 40 m s^{-1} at $z_1 = \lambda_1/4 = 1.57 \text{ km}$, but then drops off quite rapidly as the thickness of the stable layer deviates from this optimal value. Varying the height of the tropopause would cause similar fluctuations in the maximum surface velocity. However, because layer 2 has greater thickness, $|u'(0)|$ is less sensitive to changes in z_2 than to comparable variations in z_1 .

The location of the surface velocity maximum for this case is represented by the solid line in Fig. 8. As expected, for $z_1 = 1.57 \text{ km}$, the maximum surface velocity occurs halfway down the downslope. On the other hand, Fig. 8 also indicates that the velocity maximum will move further downstream if z_1 is somewhat less than optimal. Thus, even linear theory can account for some downstream displacement of the surface wind maximum although, as mentioned previously, nonlinear interactions are thought to be primarily responsible for this effect.

e. Geometrical and physical interpretations

The strong surface wind amplification produced in the optimal three-layer atmosphere can be explained with the aid of a graphical representation of the three-layer solution in the absence of mean shear. Vertical profiles of the perturbation streamfunction ψ' are plotted in Fig. 9. We have depicted these profiles (represented by solid lines) as a function of height for uniform, hydrostatic flow over a sinusoidal surface. The lower

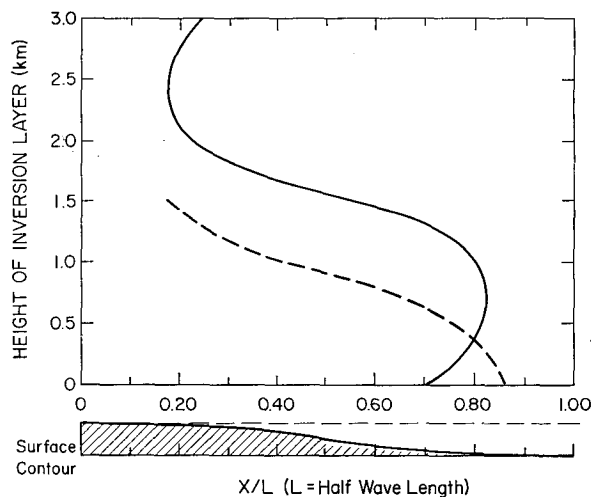


FIG. 8. Location of the surface velocity maximum for the cases plotted in Fig. 7.

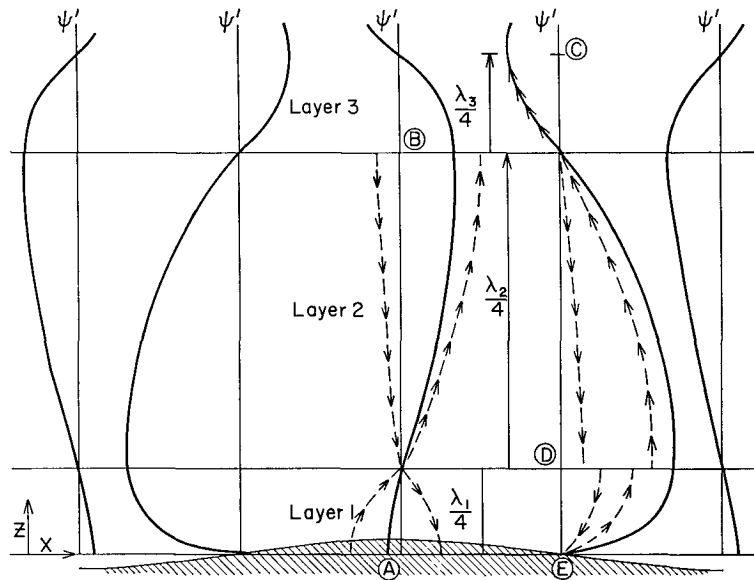


FIG. 9. Vertical profiles of perturbation streamfunction at various positions along a sinusoidal mountain contour for a three-layer atmosphere in which each of the lower two layers is one-quarter of a vertical wavelength in thickness. Solid lines represent perturbation streamfunction ψ' ; dashed lines the components of ψ' propagating wave energy upward and downward, with the arrows indicating the direction of transport.

two layers are each one-quarter of a vertical wavelength in thickness and the stabilities in layers 1 and 3 are relatively large compared to that in the middle layer. The streamfunction ψ' is negatively proportional to the displacement height, i.e., $\psi' = -U\zeta$, and at the surface, ζ is the height of the mountain. The interfacial boundary conditions [Eq. (5)] require that ψ' and $\partial\psi'/\partial z$ be continuous for $\alpha_1, \alpha_2 = 0$.

To begin, let us consider the vertical variation of ψ' above the point A, where the surface contour has its maximum height, and correspondingly where ψ' has its maximum negative surface value. Moving upward, we see that the profile for ψ' oscillates sinusoidally through a quarter wavelength in each of the lower two layers. Because the middle layer is thicker (less stable), the displacement amplitude at the tropopause (point B) will be greater than that at A by a factor of $\lambda_2/\lambda_1 = N_1/N_2$. The application of a radiation boundary condition in the top layer yields a solution characterized by wave motion of constant amplitude having lines of constant phase that tilt upstream with height. As a result, if we now view the ψ' profile one-quarter horizontal wavelength further downstream, it is evident that the magnitude of the perturbation at points B and C are the same. Coming down from point C to D, the profile again shifts through one-half wavelength, producing an amplitude for ψ' at D greater than that at C by a factor of $\lambda_2/\lambda_3 = N_3/N_2$. Consequently, the perturbation of ψ' at D is greater than its maximum amplitude at the surface (point A) by a factor of N_1N_3/N_2^2 , which is identical to the value of A_{\max} in Eq. (11). For a

single layer atmosphere with the same properties as those in layer 1, the wave amplitude throughout the atmosphere would correspond to that at point A. Since $u' = \partial\psi'/\partial z$, it is clear that the surface magnitude of u' halfway down the downslope will also be greater in the optimal three-layer system by the factor A_{\max} .

This amplification mechanism can also be interpreted in terms of the partial wave reflections which occur in a multi-layer medium having differing propagation characteristics. In each layer the solution is actually comprised of two linearly independent solutions—one propagating wave energy upward and the other propagating wave energy downward. In Fig. 9, the dashed lines depict these two components of the full solution for the perturbation streamfunction. In the uppermost layer there is no downward transport of wave energy because of the radiation condition imposed in this region. In the lower two layers, however, both upward and downward propagating modes are present, due to partial reflection of the wave motion at the interfaces between layers. This situation is analogous to other types of wave propagation in which partial internal reflections result from changes in the refractive index of the medium. In fact, defining the index of refraction to be inversely proportional to the velocity at which energy is transported, we note that the vertical group velocity for the case of uniform mean shear is given by (Bretherton, 1966)

$$C_{gz} = \pm \frac{kNl}{(k^2 + l^2)^{1/2}} \xrightarrow{k \rightarrow 0} \pm \frac{kU^2}{N}.$$

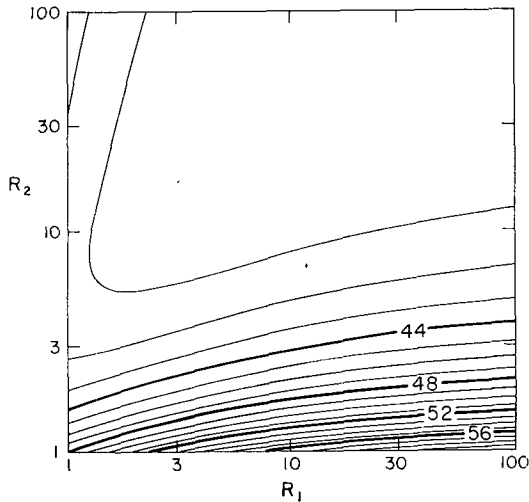


FIG. 10. Contours of the maximum perturbation surface velocity (m s^{-1}), as a function of the mean Richardson numbers, R_1 and R_2 , in the lower two layers. ($N_0 = N_2 = 0.02 \text{ s}^{-1}$, $N_1 = 0.01 \text{ s}^{-1}$).

This shows that in the hydrostatic limit the index of refraction is proportional to the stability of the layer. (For a non-uniform mean shear it is not apparent that this analogy remains meaningful.)

In the lowest layer, we can define a reflection coefficient as the squared ratio of the downward propagating wave amplitude a_1 to that of the upward component b_1 . This ratio was derived by Eliassen and Palm (1960) and for hydrostatic flow with small mean shear becomes

$$r = \frac{b_1^2}{a_1^2} = \frac{N_2^2(N_1 - N_3)^2 + (N_1^2 - N_2^2)(N_3^2 - N_2^2) \sin^2 \phi_2}{N_2^2(N_1 + N_3)^2 + (N_1^2 - N_2^2)(N_3^2 - N_2^2) \sin^2 \phi_2}.$$

As Eliassen and Palm noted, this expression represents the reflection coefficient in optics if the stability is replaced by index of refraction. For given stabilities in each layer, r depends only on the phase shift across the middle layer, and has its maximum value for $\phi_2 = \pi/2$.

When each of the lower two layers has a quarter-wavelength thickness, it can be demonstrated, by use of familiar concepts in wave reflection, that the amplitude of both the upward and downward propagating modes in the lowest layer, a_1 and b_1 , is maximized. The largest displacement perturbation then occurs halfway down the slope (see Fig. 9), where the two modes are in phase. Since the energy and momentum fluxes are proportional to $a_1^2 - b_1^2 > U_1^2 H^2$, these transports are also enhanced in an optimally layered system. This amplified energy flux can be further interpreted as an increase in the effective impedance of the system, where impedance is interpreted as the ratio of energy production to surface displacement.

f. Strong-shear case

In order to investigate how the response might be affected by the presence of substantial mean shear, we

shall briefly consider solutions to expressions (6) and (7) without neglecting any shear-dependent terms. For simplicity, a representative set of atmospheric conditions will be specified and then (6) and (7) will be evaluated for varying mean Richardson numbers in the lower two layers. Thus, we begin by setting the stabilities in the three layers to the values assumed in the previous example, which are listed in (14). For a given stability in each layer, $|\hat{u}(0)|$ depends only on R_i and ϕ_i , $i = 1, 2$. As a result, the maximum response can be determined as a function of mean Richardson number by locating the optimal phase shifts ϕ_1 and ϕ_2 , corresponding to each pair of values for R_1 and R_2 . These computations lead to the results summarized in Figs. 10 and 11. In Fig. 10, contours are plotted for the maximum value of $|\hat{u}(0)|$ as a function of R_1 and R_2 for a 1 km sinusoidal mountain contour. Recalling Fig. 7, we note that this same example produced a maximum $|\hat{u}(0)|$ of 40 m s^{-1} in the limit of large R_1 and R_2 . Thus it is apparent in Fig. 10 that the maximum surface winds obtained by including shear effects are similar to the value computed in the absence of shear, except for cases in which R_2 becomes $O(1)$ in magnitude. Within the framework of our linear shear assumption, however, the mean Richardson number in the relatively thick middle layer cannot be very small for physically realistic situations. In fact, our estimates indicate that the portion of the plot for which $R_2 \lesssim 3$ is outside physically meaningful limits. As a result, for reasonable atmospheric profiles the maximum surface wind amplitude is well represented by the value obtained in the large Richardson number limit.

The optimal thicknesses of the lower two layers are more substantially affected by shear. The values of ϕ_1 and ϕ_2 which generated the maximum response in Fig. 10

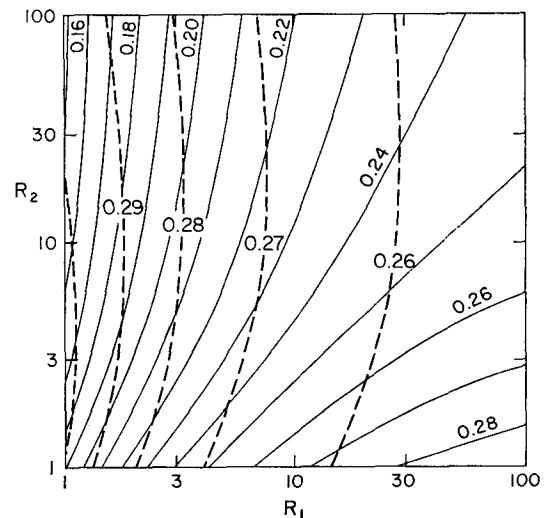


FIG. 11. Optimal phase shifts across each of the lower two layers for the cases plotted in Fig. 10: solid lines, $\phi_1/2\pi$; dashed lines, $\phi_2/2\pi$.

are shown in Fig. 11. Here we see most notably that as R_1 decreases, the optimal phase shift ϕ_1 across the inversion layer is reduced from the quarter-wavelength thickness which results when shear is neglected. On the other hand, ϕ_2 increases correspondingly, so that for all cases shown in the figure the total phase shift across the lower two layers is within 10% of one-half wavelength.

g. Four-layer solutions

Since the three-layer model described above admittedly represents a considerable idealization of the real atmospheric environment, it is of interest to investigate certain relevant modifications to this system which can be studied analytically. In particular, it is apparent that the response amplitude can depend rather critically on the detailed structure of the atmosphere in the vicinity of mountain-top level. Referring back to Fig. 3, notice that the base of the low-level stable layer in the composite soundings is located about 70 mb (or about 830 m) above the mountain-top level of 650 mb. In the thin region beneath this stable layer, the stability appears to be relatively low. Within the framework of our multi-layer analysis we have considered this situation by adding one additional layer of small stability beneath the stable layer of the three-layer system. The solution describing the wave motion in this four-layer system with small shear is obtained in just the same manner as for three layers except that one additional set of matching conditions is required to incorporate the fourth layer. Thus, by following the procedures outlined previously, we have derived an expression (not shown) exactly analogous to Eq. (8) for the maximum surface velocity generated by wave motion in the four-layer system.

For this model, we found that the maximum surface winds actually occur when the lowest layer has zero thickness, and the remaining three layers have the optimal structure described previously. Thus the potential for the greatest response occurs when the base of the inversion is at the surface and when this stable layer is one-quarter of a vertical wavelength in thickness. A rather strong or deep inversion layer is required to satisfy this criterion, however, and atmospheric soundings associated with windstorm situations indicate that the observed stable layers are often somewhat less intense. The existence of a shallow layer of low stability under the inversion has the effect of substantially reducing the optimal thickness of the inversion layer with only a moderate reduction in the predicted wind speed response. Thus, while Fig. 7 (solid curve) indicates that a reduction of the inversion depth by one-half would reduce the wind maximum by a factor of 3, we find that the presence of a less stable layer of 500 m in thickness beneath the inversion allows the inversion layer depth to be halved with only about a 25% reduction in predicted wind speed. In all

cases, however, the maximum response occurs when the total phase shift across the troposphere is very nearly one-half wavelength.

h. Neutral layer beneath a sharp inversion

To this point we have analyzed characteristics of the wave motion developing in continuously stratified atmospheric environments. Although all real stability profiles are in fact continuous, very sharp inversion layers are occasionally observed in association with strong wave response. These inversions commonly occur above a layer of low or neutral stability formed by turbulent mixing, frontogenesis, or radiative cooling processes. Thus it is important to consider the response which can be generated when a strong, almost discontinuous inversion layer exists slightly above mountain-top levels. This type of atmospheric structure is of special theoretical interest also, since it bears some similarity to the idealized atmosphere assumed when the mountain wave phenomenon is modeled using hydraulic jump theory. Our results will therefore be compared in Section 5 with hydraulic jump solutions for a simplified atmosphere.

To determine the effects of a sharp inversion, we first considered a four-layer model similar to that above in which a neutrally stable layer was added beneath the three-layer atmosphere depicted in Fig. 6. For this system it was found that if the density decrease across the lower stable layer was held constant, the optimal response amplitude kept increasing as the inversion became thinner, reaching a maximum in the limiting condition of a density discontinuity. Since the interdependence of the solution amplitude on the various layers is rather complicated in the four-layer model, we will discuss only the limiting condition of a three-layer atmosphere containing an infinitely sharp inversion. This system apparently has the greatest potential for generating a strong response if the lowest layer has nearly neutral stability and it illustrates the type of results obtained in the more general case.

The density profile considered here is presented in Fig. 12 for an incompressible atmosphere. For simplicity we have again assumed small mean shear in each layer (constant velocity in the neutral layer) and again seek solutions of Eqs. (1) subject to boundary and matching conditions (3), (4) and (5), with the following modifications. In the lowest layer, because of the neutral stability, the linear equation becomes $\nabla^2 w_1 = 0$, where ∇^2 is the Laplacian operator in the x, z plane. Also to account for the density discontinuity at $z = z_1$ the second matching condition in (5) must be altered for $i = 1$. Assuming that $\Delta\rho/\rho_0 \ll 1$, this condition now becomes

$$\frac{\partial \hat{w}_1(z_1)}{\partial z} - \frac{g'}{U_1^2} \hat{w}_1(z_1) = \frac{\partial \hat{w}_2(z_1)}{\partial z},$$

where $\Delta\rho$ is the amplitude of the density discontinuity and $g'=(\Delta\rho/\rho_0)g$ represents the reduced gravity. The solution for this system is obtained in a straightforward manner and yields the following expression for

$\hat{w}_1(z)$ in the lower layer:

$$\hat{w}_1(z) = iU_1 H(k \cosh kz + c_1 \sinh kz), \quad (15)$$

where

$$c_1 = \frac{g' N_2(\beta + \tan\phi_2) + iN_3(1 - \beta \tan\phi_2)}{U_1^2 N_2[\beta(1 - F) - F \tan\phi_2] - iN_3[F + \beta(1 - F) \tan\phi_2]}, \quad (16)$$

and

$$\beta = \frac{g'}{N_2 U_1}, \quad F = \frac{g' z_1}{U_1^2}, \quad \phi_2 = l_2(z_2 - z_1).$$

Since application of the continuity equation yields

$$\hat{u}(0) = -U_1 H c_1, \quad (17)$$

the strongest surface velocity occurs when $|c_1|$ is maximized. This maximum is achieved by first minimizing the magnitude of the denominator of (16) with respect to the parameter F , and then finding the value of ϕ_2 that maximizes the entire expression. Following this procedure we find that the maximum surface velocity occurs when

$$F = \frac{\beta^2}{1 + \beta^2} \quad \text{and} \quad \phi_2 = -\tan^{-1}\beta, \quad (18)$$

where ϕ_2 is taken in the quadrant $\pi/2 \leq \phi_2 \leq \pi$. Subject to these conditions the optimal surface wind becomes

$$\hat{u}(0) = -iN_3 H(1 + \beta^2). \quad (19)$$

This expression is precisely the same as the optimal two-layer solution derived in the discussion following expression (13), multiplied by the factor $(1 + \beta^2)$. Since typical values of β are near unity, the presence of a sharp inversion can substantially enhance the response amplitude.

Since $\hat{u}(0)$ is negative imaginary in Eq. (19), the maximum wind speed again occurs halfway down the

downslope. In the optimal configuration, F , the inverse Froude number squared, is always less than 1 and the phase shift across layer two is between one-quarter and one-half wavelength. As the strength of the inversion increases, β increases, with the result that the optimal F moves toward unity and ϕ_2 approaches $\pi/2$. In addition, by computing the solution at the tropopause, it can readily be shown that when the conditions in Eqs. (18) are satisfied, the phase shift of the wave motion between the ground and tropopause is just one-half wavelength—the same as for the optimal three-layer system discussed previously.

To illustrate the magnitude of the response predicted by this multi-layer system, we again utilize the atmospheric conditions described in (14), with the exception that $N_1 = 0$ and $g' = 0.316$, corresponding to a 10 K increase in potential temperature across the inversion. The tropopause height z_2 is set at the value for which both of the optimal conditions in (18) are satisfied. The dashed line in Fig. 7 then shows the maximum surface velocity as a function of the thickness of the neutral layer. In this case $\beta = 1.58$ and the maximum value of $|\hat{u}(0)|$ is 35 m s^{-1} , occurring at $z_1 = 0.9 \text{ km}$. Notice that again the maximum surface wind is very sensitive to small changes in the height of the inversion. Comparing the maximum amplitudes of the two curves in this figure is not particularly meaningful, however, owing to differences in the characteristics of the inversion layers. The position at which the surface velocity maximum occurs is plotted in Fig. 8 (dashed line). Here also, if z_1 is somewhat less than optimal, the location of the maximum surface wind will move further downstream.

4. Linear numerical model and real data tests

These analytic solutions provide an understanding of types of atmospheric conditions capable of producing strong wave response. These models deal, however, with idealized environments characterized by layers of constant stability and linear shear which are always an oversimplification of actual conditions. Furthermore, these analyses indicate that the wave amplitude can be quite sensitive to rather small variations in the upstream atmospheric structure. For this reason a linear numerical model has been developed in order to provide the capability of simulating real atmospheric situations and to facilitate further model testing.

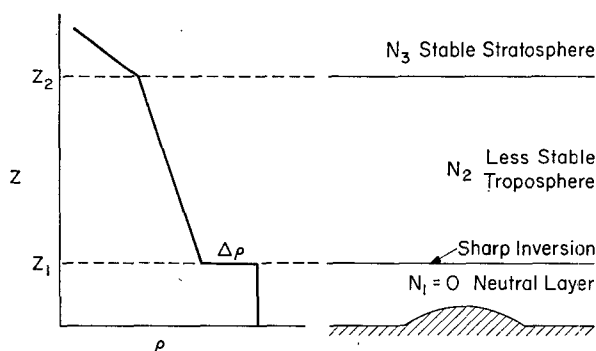


FIG. 12. Density profile for a three-layer incompressible atmosphere in which a sharp inversion is present above a low-level layer of neutral stability. The upper two layers represent the remainder of the troposphere and the stratosphere.

In constructing this numerical model, it is advantageous to use potential temperature as the vertical coordinate since this framework tends to concentrate grid points in regions of increased stability where the phase of the wave is changing most rapidly. For two-dimensional adiabatic flow the lower boundary condition can then be treated exactly, if the mountain contour is assumed to represent a constant θ surface. In addition, the governing equations are somewhat simplified by the disappearance of vertical advection terms. This coordinate system was proposed for the mountain wave problem by Krishnamurti (1964).

In the present analysis, we are concerned with steady-state, two-dimensional, isentropic flow in which rotational effects are negligible. Since we are primarily interested in the hydrostatic response, this approximation will be utilized in the derivations which follow. To test the validity of the hydrostatic assumption, however, a nonhydrostatic numerical model was also developed for comparison purposes, and some results from that model will be mentioned later in this section. Thus, subject to the above conditions, the equations of motion in θ coordinates (Lilly and Kennedy, 1973) become simply

$$-\frac{\partial}{\partial x} \left(u \frac{\partial p}{\partial \theta} \right) = 0, \quad (20)$$

$$-\frac{\partial}{\partial x} \left(\frac{1}{2} u^2 + \Phi \right) = 0, \quad (21)$$

$$\frac{\partial \Phi}{\partial \theta} = c_p \left(\frac{p}{p_0} \right)^{R/c_p}, \quad (22)$$

where

$$\Phi = c_p T + gz = c_p \theta \left(\frac{p}{p_0} \right)^{R/c_p} + gz, \quad (23)$$

Φ being the Montgomery potential. Here, (20) is the transformed continuity equation, (21) represents the horizontal momentum equation, and (22) is obtained by differentiating (23) with respect to θ and utilizing the hydrostatic approximation. Linearizing Eqs. (20)–(23) in the usual manner we can obtain, after some algebraic manipulation, a single equation in terms of one of the unknown variables. We have found it convenient to derive this equation in terms of the perturbation Montgomery potential Φ . Since the radiation-type boundary condition must be applied to each individual Fourier component, we seek a representation in terms of the Fourier transform Φ of the perturbation variable. Following this procedure then leads to the simple equation

$$\frac{\partial^2 \hat{\Phi}_1}{\partial \Theta^2} + \gamma^2 \hat{\Phi}_1 = 0, \quad (24)$$

where

$$\left. \begin{aligned} \hat{\Phi}_1 &= \left(\frac{\bar{p}}{\rho_0} \right)^{\frac{1}{2}} \hat{\Phi}, \quad \Theta = \ln \frac{\theta}{\theta_0} \\ \gamma^2 &= \frac{g}{\bar{U}^2} \frac{\partial \bar{z}}{\partial \Theta} - \frac{1}{4} \left(1 - \frac{c_v}{c_p} \frac{\partial \ln \bar{p}}{\partial \Theta} \right)^2 - \frac{1}{2} \frac{c_v}{c_p} \frac{\partial^2 \ln \bar{p}}{\partial \Theta^2} \end{aligned} \right\}. \quad (25)$$

Here an overbar refers to the mean state and a zero subscript denotes the undisturbed value at ground level.

At the surface, $\Theta=0$, the mountain contour is a prescribed function of x . Thus, combining (22) and (23), we require that

$$\hat{\Phi} - \frac{\partial \hat{\Phi}}{\partial \Theta} = g \hat{z}_0 \quad \text{at } \Theta=0, \quad (26)$$

where \hat{z}_0 is the Fourier transform of the actual mountain contour. In order to permit the upward propagation of wave energy through the top of our domain of interest, we assume that above a certain level, $\Theta=\Theta_T$, the atmosphere has constant propagation characteristics. Therefore, γ will have a constant value γ^* above $\Theta=\Theta_T$, allowing downward energy flux to be eliminated in this region by applying the radiation boundary condition

$$\frac{\partial \hat{\Phi}}{\partial \Theta} = i \gamma^* \operatorname{sgn}(k) \hat{\Phi} \quad \text{at } \Theta=\Theta_T, \quad (27)$$

with Θ_T being located at an appropriate level in the lower stratosphere. Rewriting (26) and (27) in terms of $\hat{\Phi}_1$ then yields the lower and upper boundary conditions

$$\frac{1}{2} \left(1 + \frac{c_v}{c_p} \frac{\partial \ln \bar{p}}{\partial \Theta} \right) \hat{\Phi}_1 - \frac{\partial \hat{\Phi}_1}{\partial \Theta} = g \hat{z}_0 \quad \text{at } \Theta=0, \quad (28)$$

$$\frac{\partial \hat{\Phi}_1}{\partial \Theta} - i \gamma^* \operatorname{sgn}(k) \hat{\Phi}_1 = 0 \quad \text{at } \Theta=\Theta_T. \quad (29)$$

In deriving (29), it is assumed that $\partial \ln \bar{p} / \partial \Theta$ is continuous across $\Theta=\Theta_T$.

For any particular mountain shape, the solution is derived by computing the Fourier transform of the surface contour, solving the differential equation (24) subject to the boundary conditions (28) and (29), and finally taking the inverse transform of the resulting solution. [Note that owing to the hydrostatic assumption, Eq. (24) need only be solved twice—once for positive k and once for negative k .] This procedure implicitly assumes periodic boundary conditions in the horizontal direction. However, since the long-wave response drops off rapidly both up- and downstream of the mountain, the effects of periodicity are minimal when the outer boundary is located far from the mountain.

To illustrate a solution generated by the numerical model, we have depicted in Fig. 13 the wave motion

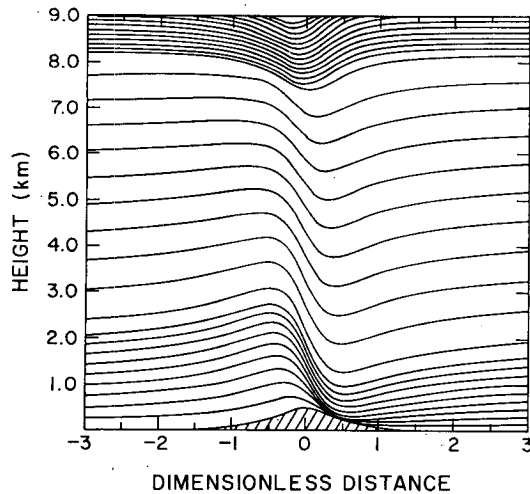


FIG. 13. Linear streamline pattern for flow past a bell-shaped mountain. The mean state of the atmosphere has a three-layer structure described by the conditions of Eq. (12). The vertical spacing of streamlines in the unperturbed flow is inversely proportional to the square of the stability N .

generated by a bell-shaped mountain in an atmosphere whose mean state corresponds to the optimal three-layer structure described in the previous section by the conditions in (12). For this case, the horizontal boundaries were set at $x/L = \pm 6$, where L represents the mountain half-width. (For hydrostatic flow, the solution to the dimensionless equations is independent of the horizontal length scale, and thus L only provides a scaling factor for the solution.) The streamlines plotted in this figure are separated by equal increments in Θ (a total of 100 grid points were used in the vertical) and thus more closely spaced streamlines reflect a region of increased stability. Here the wave amplitude at the top of the inversion layer is about $3\frac{1}{2}$ times the maximum (500 m) height of the mountain, revealing the strong amplification produced by a "tuned" three-layer atmosphere.

In this example, the quarter-wavelength phase shift across each of the lower two layers can be clearly observed. Notice, however, that within each layer the phase shift is not uniform with height. In the lowest layer the phase shifts most rapidly just above the ground, while in the middle layer most of the phase shift occurs near the tropopause. The reasons for this are clear if we return momentarily to the analysis of the previous section for a single horizontal wavenumber k . For the optimal three-layer system with small vertical shear, it can readily be shown that

$$\left. \begin{aligned} kx + \tan^{-1} \left[\frac{N_1 N_3}{N_2^2} \tan l_1 z \right] &= \text{constant} \quad \text{in layer 1} \\ kx + \tan^{-1} \left[-\frac{N_3}{N_2} \cot l_2 (z - z_1) \right] &= \text{constant} \quad \text{in layer 2} \end{aligned} \right\}, \quad (30)$$

which is in contrast to the expression $kx + lz = \text{constant}$, valid in an atmosphere having uniform properties. The phase shifts given in (30) are consistent with those observed in Fig. 13.

In Fig. 13 we note the very close packing of streamlines near the lee slope. As the wave amplitude increases, adjacent streamlines will begin to cross over each other. This is clearly unrealistic and is caused by applying the linear solution to situations in which nonlinear effects are obviously significant. Nevertheless, as mentioned previously, linear theory provides a valuable tool for identifying the atmospheric conditions capable of producing a strong response and for investigating the basic dynamics of wave motion.

To this point we have not considered the influence of the mountain shape on the resulting response amplitude. Although the atmospheric structure appears to control the response potential, the mountain's shape, as well as its height, will influence the actual wave amplitude for a given atmospheric environment. To demonstrate this effect, we have computed from the optimal three-layer atmosphere specified by Eq. (12) the perturbation surface velocity profiles for two rather different mountain shapes. In the first case, shown by solid lines in Fig. 14, the mountain profile is just one cycle of a sine wave. The second mountain contour (denoted by a dashed line) is similar to the first, except that on the upstream side, the mountain height drops off very gradually to zero. Bretherton (1969) has pointed out that the solution diverges for a nonperiodic ramp-shaped mountain. This ramp- or plateau-shaped mountain is roughly analogous to the situation west of Boulder, where the Rocky Mountains extend far upstream of the Continental Divide and flow at lower levels in this region often appears to be at least partially blocked. From Fig. 14 we see that the maximum surface wind produced by the ramp-shaped mountain is about 50% greater than the corresponding maximum for the isolated, symmetrical mountain. For comparison, the solid horizontal bar indicates the value of $|\hat{u}(0)|$ for a continuously sinusoidal mountain having the same height. These results, though by no means conclusive, suggest an additional factor, mountain shape, which may contribute to the generation of intense downslope winds on the eastern slope of the Rocky Mountains.

Using the linear numerical model, we can attempt to simulate the real atmosphere by utilizing the appropriate upstream sounding data to define the mean state in the model. As an initial test, this simulation was performed for the 11 January 1972 windstorm in Boulder. Using a 2 km ramp-like mountain contour in the model, and an upwind sounding constructed from the aircraft data and the 0000 GMT 12 January Grand Junction rawinsonde, we obtained the wave solution shown in Fig. 15. Here the very large amplitude streamlines pass right through the surface of the mountain, again indicating that linear theory has been pushed far beyond its proper limits. However, in the

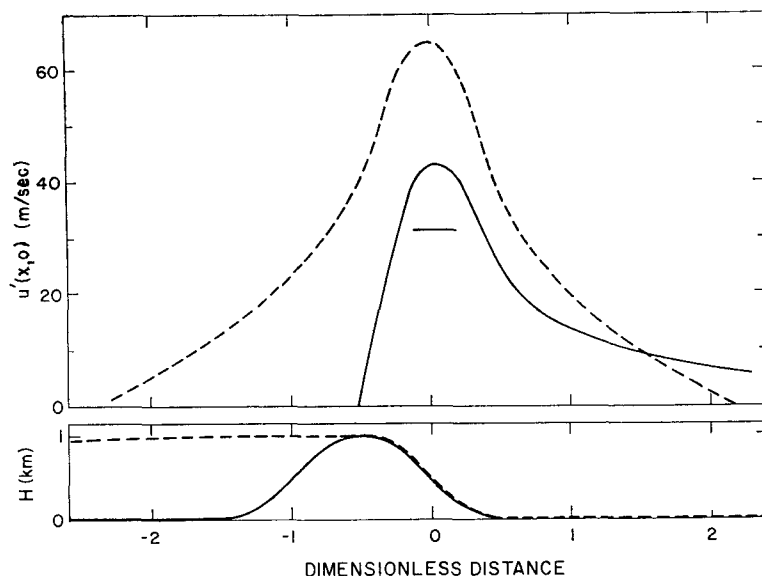


FIG. 14. Perturbation surface velocity profiles for two different mountain shapes. The solid line is a mountain contour represented by one cycle of a sine wave; the dashed line a ramp-shaped mountain with height gradually dropping off to zero far upstream. The solid horizontal bar indicates the maximum velocity produced by a continuously sinusoidal mountain of the same height.

middle troposphere, this simulation appears to model the essential features of the large-amplitude wave observed on that day (see Fig. 4).

To test the possible importance of non-hydrostatic effects, the 11 January 1972 case was also simulated using a non-hydrostatic version of the model, specifying the distance from the mountain crest to the base to be 30 km. Without describing the details of the non-hydrostatic model, we will just mention that the solution was virtually the same as the hydrostatic one except that its displacement amplitude was reduced by about 6%. This result is typical of several other cases which were also tested.

If the linear numerical model can produce simulations which exhibit wave amplitudes proportional to those actually occurring in the atmosphere, it could provide a valuable tool in forecasting periods of intense wave activity and the associated downslope winds. To investigate this possibility, a large number of real data cases were simulated and predicted responses were compared to actual developments. For this study, sounding data at 12 h intervals were collected from upstream National Weather Service rawinsonde stations for most of the 20 windstorm cases analyzed by Brinkmann (1973) and also for the entire month of January 1972, which was a particularly windy month in Colorado, but with intermittent quiet periods.

Quite frequently, the available upstream sounding stations are not in the desired upwind location. Often the upwind direction falls somewhere between Grand Junction and Lander, with Salt Lake City too far west for the sounding to be used with much confidence. For

this reason, a computerized cross section analysis (Shapiro and Hastings, 1973) was performed for these cases along a north-south line about 300 km west of Boulder. The sounding was then taken from the appropriate position along the cross section and entered as the mean state in the numerical model. Eighty Θ levels were used in the vertical, which was sufficient to accurately represent the sounding profiles and produce a solution invariant to further decreases in $\Delta\Theta$.

For comparison purposes the only data consistently

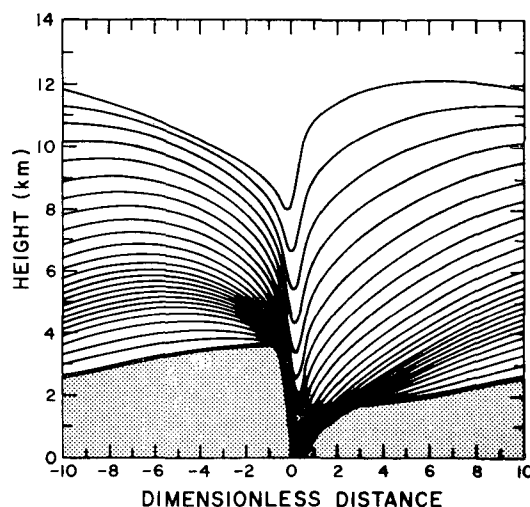


FIG. 15. Linear streamline pattern for flow over a ramp-shaped mountain using observed upstream data from 11 January 1972 to specify the mean state.

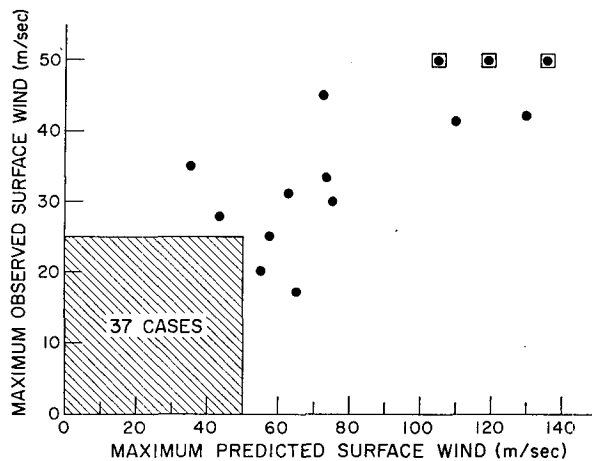


FIG. 16. Comparison of the maximum predicted surface winds with the maximum recorded by the Southern Hills anemometer in the interval 2–5 h after the soundings were taken. A box around a data point indicates that the recorder pegged at 100 mph.

available are measurements of the surface winds experienced in Boulder. Thus for each case considered the maximum surface wind predicted by the model was compared with the maximum gust intensities recorded at an anemometer station in south Boulder in the period 2–5 h after the upstream soundings were taken. This maximum surface wind generated by the inviscid numerical model presumably corresponds to a steady wind just above the turbulent boundary layer near the ground. However, there is some evidence to suggest that this wind speed should be comparable to the maximum gusts occurring at the surface.

The choice of a 2–5 h lag time for verification purposes was made somewhat arbitrarily because it seemed to produce the best correlation. Because of this choice, however, we could not test the model against all windstorm events using sounding data obtained every 12 h. However, it should be emphasized that the purpose was to test the model's reliability in simulating the response associated with a determinable upstream environment rather than to try to explain all the observed periods of strong activity. To further facilitate this model testing, cases were discarded if the estimated wind direction in the mid-troposphere deviated by more than $\pm 30^\circ$ from westerly or if variations in wind direction between different stations or levels caused a significant uncertainty in fixing the appropriate wind direction. Thus, of the 88 sets of sounding data in the initial sample, 37 were eliminated on the abovementioned basis of wind direction. Of these, three correspond to winds exceeding 35 m s^{-1} in Boulder. More complete details pertaining to the model testing will be presented in a separate report.

The results from these real data simulations are summarized in Fig. 16. Each point corresponds to a separate case and indicates both the maximum predicted surface wind (abscissa) and the actual maximum

gusts recorded 2–5 h later by the South Boulder anemometer (ordinate). Notice that the model tends to overpredict the response by about a factor of 2. This is not surprising since the instability and turbulent breakdown of large-amplitude waves are not accounted for in the linear model. Furthermore, it is not too disturbing since the real goal here is only to determine whether a strong positive correlation exists between the predicted and observed response. Cases for which the wind gusts in Boulder were less than 25 m s^{-1} and the model predicted less than 50 (corresponding to the shaded area in Fig. 16) were not plotted, since the indicated mountain wave activity is weak and often not a primary factor in producing the observed winds. Points with boxes around them indicate that the recorder needle pegged at 100 mph, and they were arbitrarily plotted as 50 m s^{-1} .

From data plotted in Fig. 16, a strong positive correlation between predicted and observed maximum winds is apparent. For example, in all six cases for which wind gusts in Boulder exceeded 40 m s^{-1} , a very strong response was predicted by the model. In addition, there are no cases which grossly over- or underpredict the response. The good correspondence between predicted and observed winds is very encouraging, and suggests that the model can provide a valuable contribution toward forecasting this phenomenon from a knowledge of the structure of the upstream environment. Because of the relatively few strong wind cases analyzed thus far, however, further model testing must be conducted before definite conclusions can be drawn.

As mentioned in Section 3, the phase shift across the troposphere was very nearly one-half wavelength for all of the optimally structured multi-layer systems that were considered. This result is also emphasized in our real data simulations and is summarized in Table 1. Here we see the strong tendency for strong predictions to have a half-wavelength phase shift, while weaker cases are associated more with one-quarter or three-quarter phase shifts.

5. Comparison with hydraulic jump models

It is clear that our approach to the downslope windstorm problem bears little or no resemblance to the hydraulic jump theory espoused by a number of previous investigators. The attractiveness of the jump

TABLE 1. Correlation between predicted phase shift across troposphere and maximum surface wind.

Phase shift across troposphere	Maximum predicted surface wind (m s^{-1})		
	<50	50–75	>75
$\frac{1}{4}\lambda$	15		
$\frac{3}{4}\lambda$	5	1	
$\frac{1}{2}\lambda$		4	6
$\frac{5}{4}\lambda$	3	1	
$\geq \frac{3}{2}\lambda$	16		

model is evident enough, however, from a cursory inspection of the lower level structure of the 11 January 1972 windstorm, which shows a sudden uplifting of the low-level flow together with the generation of strong turbulence. In addition, the observational ubiquity of strong low-level stability is attractive to jump modelers. Because the upper tropospheric features of the 11 January case appear to be more consistent with wave than jump dynamics, and in view of the apparent success of our numerical model in "predicting" strong windstorms, we are convinced of the basic validity of our results. We have, however, performed some additional analyses in an attempt to clarify the point.

A basic element of hydraulic jump theory is the non-existence of continuous finite-amplitude solutions for a certain range of Froude number when the ambient fluid consists of one or more constant density layers in steady motion. Even the linear solution becomes singular at $F=1$. It is important to recognize, however, that the linear singularity no longer exists if the fluid above the density discontinuity is continuously stratified and is subject to a radiation boundary condition. The last of our results of Section 3 was obtained for the case of a sharp inversion in the lower atmosphere, yet solutions are available for all values of the Froude number.

To point out more sharply the discrepancy between these two approaches, we consider a further simplified representation of the atmosphere, one consisting of two layers separated by a density discontinuity. In Fig. 12 this corresponds to the case $N_2=N_3=N$. For this two-layer system Eq. (17) subject to (16) reduces to

$$\hat{u}(0) = -\frac{g'H}{U} \frac{1+i(lz_1/F)}{(1-F)+ilz_1}, \quad (31)$$

where we recall that $l=N/U$. This result is identical to the solution of the linear shallow water equations if l is set equal to zero.

In the linear shallow water analysis, it is clear from (31) with $l=0$ that the solution becomes singular for a Froude number of unity. Examining the nonlinear shallow water equations for the situation, one must postulate that a hydraulic jump (a discontinuity in the height of the inversion surface) occurs in order to obtain a solution (see, e.g., Houghton and Isaacson, 1968). If, however, there is a small but nonzero stability in the atmosphere above the sharp inversion, there is no singularity in the solution, and thus linear theory is uniformly valid for all Froude numbers.

Since the development of a hydraulic jump involves nonlinear processes, it is perhaps more meaningful to compare nonlinear solutions for this simple two-layer atmospheric structure. To this end a nonlinear, time-dependent numerical model for mountain waves in a compressible atmosphere developed by the authors (to be presented in a subsequent paper) was slightly altered to allow the presence of a sharp inversion and neutral

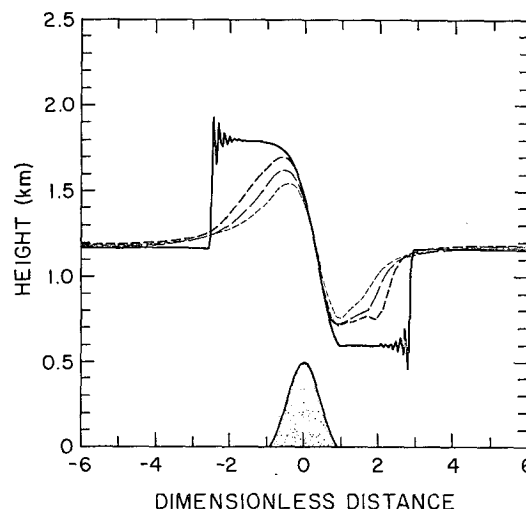


FIG. 17. Position of the inversion surface at the dimensionless time $tU_0/L=10$ for differing stabilities above the inversion, as obtained from nonlinear numerical solutions. In all cases, $U = 20 \text{ m s}^{-1}$, $F=1$ and there is a 10 K increase in potential temperature across the inversion interface with neutral stability below. The temperature lapse rate α (K km^{-1}) above the inversion are as follows: solid (neutral stability), 9.8; light-dashed, 9; heavy long-dashed, 8; heavy short-dashed, 6.

layer beneath the region of stable stratification. In addition, the nonlinear, time-dependent shallow-water equations were programmed to provide the corresponding solution for the case of neutral stability above the inversion. For these numerical experiments, the mountain height is 0.5 km and the undisturbed atmosphere is characterized by a constant mean wind of 20 m s^{-1} and a 10 K increase in potential temperature across the inversion. The Froude number was set at unity, which then required that $z_1=1.17 \text{ km}$. Under these conditions, integration of the shallow-water equations produces both upstream and downstream propagating jumps, which are depicted by the solid line representing the height of the inversion surface in Fig. 17 at a dimensionless time of 10 (corresponding to about one-half hour for a 20-km wide mountain). As time increases, these jumps continue to travel away from the mountain. A small amount of viscous damping was included in the solution in order to assure computational stability and to allow dissipation of energy in the jump. The oscillations which appear behind the jump then represent small remnants of the damped numerical instabilities. This numerical simulation then provides a solution for the simple two-layer system described above when there is neutral stability, or a lapse rate of about 9.8 K km^{-1} above the inversion. The results are very similar to those of Houghton and Isaacson, as they should be since the numerical models are also very similar.

For comparison purposes we obtained nonlinear solutions for the same two-level structure but with nonzero stability above the inversion surface. These solutions

were generated by the nonlinear wave model using various sub-adiabatic lapse rates above the inversion. In Fig. 17 the corresponding position of the inversion surface is plotted for lapse rates of 9, 8 and 6 K km⁻¹. Notice that as the stability above the inversion increases, the solution begins to deviate significantly from the jump solution. Also, for the simulations with $N^2 > 0$, the inversion surface tends to a steady-state position; for a 6 K km⁻¹ lapse rate, the steady-state solution does not differ significantly from that shown in Fig. 17 at $T = 10$. This result is in contrast to the solution for $N^2 = 0$ in which the jumps continue to propagate with time.

The differences in the character of the solutions for $N^2 = 0$ and $N^2 > 0$ can perhaps be explained in terms of energy transport. Since a hydraulic jump marks the transition from supercritical to subcritical flow, energy must accumulate at this point and thus the jump is a turbulent region in which this energy is dissipated. No energy can be propagated vertically because the upper boundary condition is reflective. If the region above the inversion has nonzero stability, however, energy can be propagated vertically out of the potential jump region by the pressure forces associated with wave motion in the stably stratified environment. Thus for $N^2 > 0$, energy is no longer trapped at this inversion surface and can radiate vertically. From our numerical experiments it appears that this additional degree of freedom can significantly alter the flow and may effectively eliminate jumps in the solution.

For very large amplitude wave motion, the wave may also propagate downstream with time, as will be discussed in more detail in a subsequent paper, if turbulent dissipation is allowed for in the wave simulation model. Thus vertical radiation of wave energy may not always be sufficient to completely remove a jump. This is consistent with the fact that energy dissipation is proportional to the cube of the jump height while the vertical energy flux is only proportional to the square. In the 11 January windstorm evidence from anemometer records indicated that the front edge of the strong winds was not only sharp but that it propagated forward continuously during the early part of the storm. Such sequences have also been observed in other storms. Yet the propagation is not indefinite, as it is in both the hydraulic jump and dissipating wave models, and strong winds seldom extend more than 25 km east of the foothills. Thus something important is lacking in all of these models, and we suspect it to be surface friction. The deceleration of the low-level winds by turbulent drag will certainly tend to thicken the boundary layer and may lead to turbulent boundary layer separation—a phenomenon which could explain the structure observed on 11 January better than can hydraulic jump theory.

The above discussion is not meant to imply that hydraulic jumps do not occur in the atmosphere, nor

that strong wave and downslope windstorms do not exhibit some aspects of jump behavior. Rather, it is felt that hydraulic jump analyses require idealized simplifications of the atmosphere which may produce artificial or misleading results. The analysis presented here emphasizes the sensitivity of the nature of the wave motion to the detailed structure of the atmosphere and indicates that care must be taken to include its essential features in modeling the mountain wave phenomenon. In particular, our theoretical and observational results emphasize the importance of the entire troposphere and lower stratosphere and the vertical propagation of wave energy in producing strong wave response.

6. Summary and conclusions

We have analyzed simple multi-layer representations of the atmosphere and demonstrated how a mountain wave and its associated surface winds can be strongly amplified if the upstream wind and stability profiles lie within sharply limited but plausible ranges. These results emphasize the fundamental role of the inversion layer frequently observed above mountain tops in generating a large-amplitude response. The mechanism which leads to this strong amplification is shown to be associated with the partial reflection of upward propagating wave energy by variations in thermal stability. In contrast to the complete reflection of short gravity waves which occur when the Scorer parameter decreases with height, the partial reflection of long waves does not lead to a resonant mode; rather, the vertically propagating wave can under certain conditions have greatly enhanced energy transport for a given forcing displacement. Thus it is appropriate to regard the partial reflection mechanism as a method of increasing impedance.

Application of a numerical version of our theoretical model to the prediction of observed maximum surface winds, using available upstream sounding data, shows an encouraging degree of success. The numerical simulations from real data also exemplify many of the results of the analytic theory. In particular, there is a strong correlation of large-amplitude response with one-half wavelength phase shifts across the troposphere. Based on these results we believe that our linear, hydrostatic, two-dimensional and steady-state model captures the essence of the downslope windstorm phenomenon, at least as observed near Boulder, and we hope that it may lead to improved operational windstorm forecasts.

In considering the relationship of our solutions to hydraulic jump theory, we find that small deviations from the idealized upstream atmospheric structure associated with jump-type solutions can substantially alter or remove the jump. Thus, we conclude that the hydraulic jump approach is too restrictive in its assumptions to properly account for the observed phenomena.

Acknowledgments. The authors would like to express their gratitude to William Bergen for his assistance in testing the forecast accuracy of our model, and to Patrick Kennedy who prepared the observational material for the 11 January 1972 windstorm. The National Center for Atmospheric Research is sponsored by the National Science Foundation.

REFERENCES

- Aanensen, C. J. M., 1965: Gales in Yorkshire in February 1962. *Geophys. Mem.*, **14**, 1-44.
- Arakawa, S., 1969: Climatological and dynamical studies on the local strong winds, mainly in Hokkaido, Japan. *Geophys. Mag.*, **34**, 359-425.
- Blumen, William, 1965: A random model of momentum flux by mountain waves. *Geophys. Publ.*, **26**, 1-33.
- Bretherton, F. P., 1966: The propagation of groups of internal gravity waves in shear flow. *Quart. J. Roy. Meteor. Soc.*, **92**, 466-480.
- , 1969: Momentum transport by gravity waves. *Quart. J. Roy. Meteor. Soc.*, **95**, 213-243.
- Brinkmann, W. A. R., 1973: A climatological study of strong downslope winds in the Boulder area. NCAR Cooperative Thesis No. 27, University of Colorado, 229 pp.
- Eliassen, A., and E. Palm, 1960: On the transfer of energy in stationary mountain waves. *Geophys. Publ.*, **22**, 1-23.
- Georgii, W., 1954: Studie über den Zondawind der Kordillere von Mendoza. *Meteor. Rund.*, **7**, 125-129.
- Houghton, D. D., and E. Isaacson, 1968: Mountain winds. *Stud. Num. Anal.*, **2**, 21-52.
- , and A. Kasahara, 1968: Nonlinear shallow fluid flow over an isolated ridge. *Commun. Pure Appl. Math.*, **21**, 1-23.
- Julian, L. T., and P. R. Julian, 1969: Boulder's winds. *Weatherwise*, **22**, 108-112.
- Krishnamurti, T. N., 1964: The finite-amplitude mountain wave problem with entropy as a vertical coordinate. *Mon. Wea. Rev.*, **92**, 147-160.
- Kuettner, J., 1959: The rotor flow in the lee of mountains. GRD Res. Notes No. 6, AFCRL, Bedford, Mass.
- Lilly, D. K., and P. J. Kennedy, 1973: Observations of a stationary mountain wave and its associated momentum flux and energy dissipation. *J. Atmos. Sci.*, **30**, 1135-1152.
- , and E. J. Zipser, 1972: The front range windstorm of 11 January 1972—a meteorological narrative. *Weatherwise*, **25**, 56-63.
- Scorer, R. S., and H. Klieforth, 1959: Theory of mountain waves of large amplitude. *Quart. J. Roy. Meteor. Soc.*, **85**, 131-143.
- Shapiro, M. A., and J. T. Hastings, 1973: Objective cross-section analyses by Hermite polynomial interpolation on isentropic surfaces. *J. Appl. Meteor.*, **12**, 753-762.
- Yoshino, M. M., 1971: Die Bora in Jugoslawien: Eine synoptische-klimatologische Betrachtung. *Ann. Meteor.*, **5**, 117-121.